

Anchoring of Turbulent Premixed Hydrogen/Air Flames at Externally Heated Walls

Sebastian Klukas, Marcus Giglmaier, Nikolaus A. Adams

Technical University of Munich

Moritz Sieber, Sebastian Schimek, Christian O. Paschereit

Technical University of Berlin

Abstract

A joint experimental and numerical investigation of turbulent flame front anchoring at externally heated walls is presented. The phenomenon is examined for lean hydrogen/air mixtures in a novel burner design, which comprises a cylindrical burning chamber converging into a glass pipe as well as a wall heating assembly at their intersection. The transparent part allows for optical OH^* chemiluminescence measurements serving as a basis for numerical validation.

For a comprehensive numerical evaluation the effect of heat loss on different hydrogen/air chemical reaction mechanisms is reviewed in a preparatory one-dimensional flame study. The subsequent numerical investigation focuses on the application of the Eddy Dissipation Concept (EDC) as a turbulence-chemistry interaction model in the realm of wall anchoring turbulent flames. All simulations are based on the Reynolds time-averaged formulation of the Navier-Stokes equations and feature axisymmetric domains. The influence of different two-equation turbulence models and EDC modeling constants are discussed. Since wall heat transfer is responsible for ignition as well as quenching of the flame front, a special focus is put on boundary layer resolving near-wall treatment. A qualitative comparison between simulations and experiment is performed for multiple operating conditions. These are selected to display the influence of equivalence ratio, bulk Reynolds number and unburnt mixture temperature.

While the choice of RANS-based turbulence model has a distinguishable impact, EDC modeling coefficients exhibit a more significant influence on flame shape and length. It is only surpassed by the impact of correct diffusion treatment on reacting lean hydrogen/air mixtures. To depict this behavior as accurately as possible, full multicomponent diffusion treatment using the Maxwell-Stefan equation is applied.

Keywords: Anchoring flames, wall heat transfer, hydrogen/air kinetic, EDC, wall modeling

^{*}Fully documented templates are available in the elsarticle package on CTAN.

1. Introduction

Controlled flame anchoring is often a necessary prerequisite for continuous combustion devices. Exemplary applications range from micro-combustors over jet engines to scramjets [1] [2] [3]. In general, flame anchoring may be realized by three different means of flow control: recirculation, supersonic shocks or heat transfer. Recirculation-based flame holding is either induced by wall cavities [4] [5] or bluff bodies [1] [6], which both come in various shapes and forms. Shock-induced combustion applications utilize the enhanced thermodynamic state after a shock wave to continuously ignite a mixture [7]. In addition, heat abduction, for example in form of porous media [8], or heat introduction by external means may lead to flame anchoring as well. While the latter concept has been comprehensively studied for laminar flames and micro-combustion applications [9] [10] [11], it is relatively unexplored for turbulent flames in the macroscopic scale. This study aims to supply a first insight into this problem. Flame stabilization by thermal heat induction is categorized as excess enthalpy combustion [12]. It describes the behavior of a flamelet in a continuously perfused duct or pipe and especially its thermal interplay with the adjacent walls. In this configuration excess heat of the burnt gas is conducted through the wall back to the unburnt gas, thereby heating the unburnt mixture and extending its flammability limit. The detailed behavior depends on the heat transfer coefficient between fluid and solid, heat conduction capability of the solid as well as its thermal capacity. Without any external means of heating the flame front tends to advance back and forth as well as extinguish and re-ignite periodically [10]. To remedy this issue, external heat induction to the wall leads to a less sensitive flame-wall interaction and allows for spatial control of the flame front. The general effect has been studied with a particular focus on laminar flames [11] [10].

The objective of the present investigation is to examine this flame anchoring mechanism both experimentally and numerically. Special attention is put on turbulent flame fronts and the interplay between turbulence, reaction pace and wall quenching. For this purpose a novel burner design is developed. It features an elevated turbulence degree inferring highly non-uniform local flame speeds which makes quasi-steady flame anchoring challenging. An obstacle the employed external heat induction helps to overcome. For the numerical part the interaction of turbulence and chemistry is prioritized. As a well-established model for turbulent reaction term evaluation in the RANS-context the eddy dissipation concept is employed.

One of the benefits of a flame holder based on excess enthalpy is that very lean stable burning conditions are implementable. That is one reason why this investigation features ultra-lean combustion. The low equivalence ratio reduces flame speed and allows for moderate flow velocities as well as bulk Reynolds numbers. In addition, it leads to weakened NO_x production and flame temperatures benefiting corrosion behavior as well as environmental concerns. Hydrogen fuel is employed and combined with air as an oxidizer. Besides being one of the most interesting fuels for future clean energy solutions, hydrogen combustion introduces very high flame speed. Thus, the experimental burner features elevated Reynolds numbers besides ultra-lean air-fuel ratios.

After presentation of the newly designed burner and its operating conditions, the paper is structured as follows. First, a review of the applied numerical method and especially

the EDC is exercised. Secondly, different kinetic mechanisms for hydrogen/air combustion are examined and compared with respect to their ability to portray heat losses as induced by adjacent walls. Thirdly, the influence of turbulence models, and EDC parameters on flame shape and simulation results in general are discussed. Finally, varying operating conditions displaying the impact of equivalence ratio, bulk Reynolds number as well as unburnt mixture temperature are reviewed.

2. Experimental setup

To investigate anchoring of turbulent flames at preheated walls, a novel burner design is implemented and tested thoroughly. The device is constructed to operate under a wide range of equivalence ratios, inlet mass flows and unburnt mixture temperatures. The detailed experimental setup, employed measurement techniques and operating conditions are described in this section.

2.1. Burner design and instrumentation

The burner design primarily features a converging steel tube transitioning into a quartz glass pipe (Fig. 1). At their intersection a heating assembly provides the means to control the amount of externally introduced heat into a distinct part of the stainless steel wall. During operation preheated air is injected into the steel tube at adjustable temperature and mass flow conditions. Subsequent to its injection, the air flow is straightened by increasingly narrow grids to reduce turbulent velocity fluctuations. Further downstream, right after a converging part, hydrogen is inserted radially through six injection ports equally spaced in circumferential direction. Since fuel is introduced at room temperature, the settled mixture's temperature stays below the preheated air's temperature. The distance between fuel injection and flame position is designed to justify the assumption of a perfectly premixed flame. This is confirmed by non-reacting three-dimensional CFD simulations.

The heating assembly comprises four electric heating plugs connected to a heating ring as well as insulation bands. Therefore, the heating partially replaces the chamber wall while insulation inhibits heat conduction to adjacent parts (Fig. 1). Equal spacing of the heating plugs ensures an uniform temperature distribution within the ring and thus symmetrical flame positioning. Hence, a distinctive locally heated wall is devised. The design is optimized to avoid unnecessary wall gaps in order to diminish disturbance of the turbulent boundary layer.

Total axial dimension of the burner amounts to 1.5 m. The respective wall thicknesses of the steel tube and glass pipe are 5 mm and 7.5 mm. To minimize wall heat loss before ignition an additional layer of stone wool insulation is attached to the outside stainless steel parts. Temperature measurements confirm that no significant wall heat loss takes place upstream of the heating assembly. The installed heating ring extends for 24 mm and is placed 20 mm in front of the glass tube. To chill down any hot exhaust gases a liquid cooled pipe is attached glass tube's end. The axial point of origin ($x = 0$) is placed right at the beginning of the flameholder to simplify comparison of experimental and numerical data.

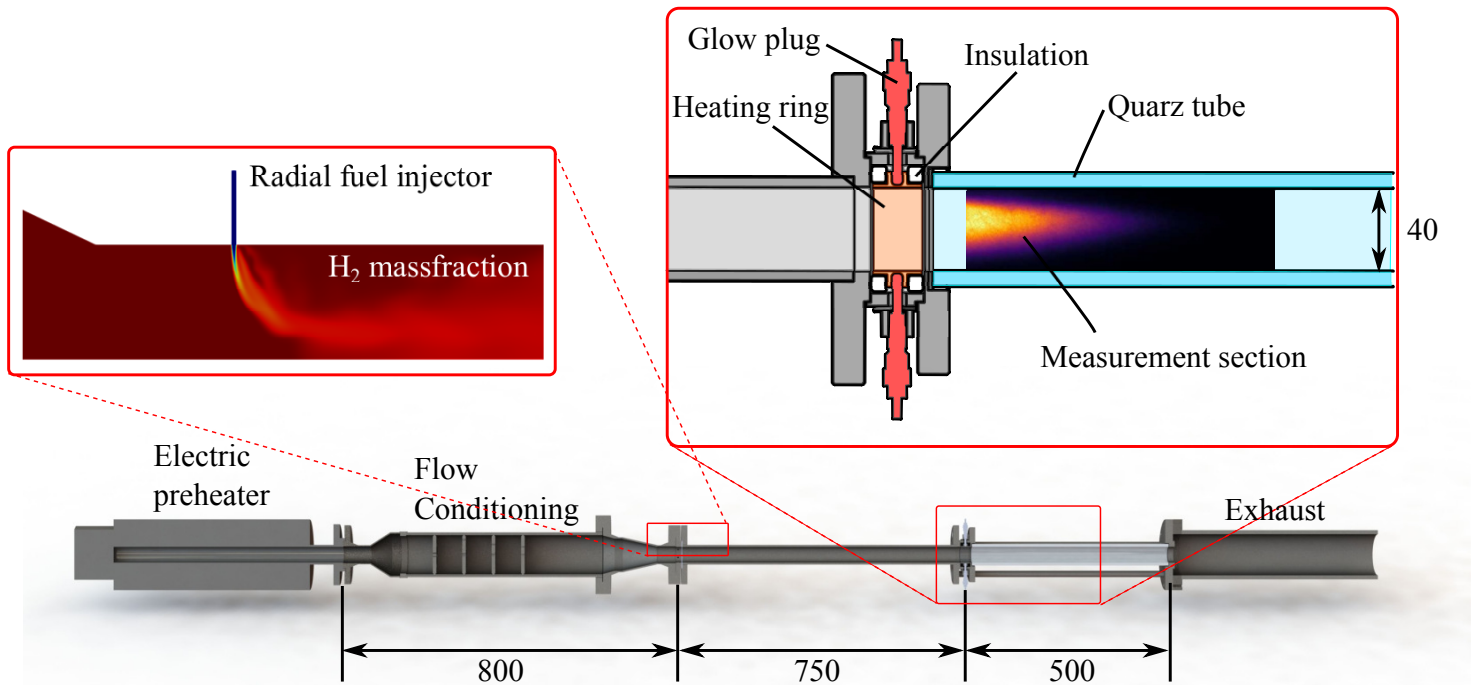


Figure 1: Schematic of the experimental burner setup. Axial dimensions are not to scale. Measuring range is marked by red box.

The measurement setup provides the means for a qualitative comparison between numerics and experiment. For this purpose relevant boundary conditions as well as the flame's reaction zone are quantified and evaluated. Air and hydrogen inlet mass flow rates are registered by a set of integrated mass flow controllers. Temperature measurements of the fluids are gained by thermocouples placed at the burner's axis. Five axial locations are selected for this purpose. The heating ring is equipped with additional thermocouples to determine the heated wall's temperature. Equal temperature distribution inside the ring is confirmed visually. To assess general flame shape and quantify the position of the reaction front, a digital camera equipped with an image intensifier is utilized. By appliance of an optical filter transmitting a wavelength from 305 nm to 315 nm the hydroxyl radical (OH^*) chemiluminescence is recorded. For each configuration 500 images are recorded at a rate of 5 Hz and averaged to obtain an accurate representation of the mean flame shape.

2.2. Operating conditions

One of this study's objectives is to investigate the influence of three major reactive flow characteristics and their effect on burner stability and overall flame shape. Those are: equivalence ratio, inlet mass flow rate and unburnt mixture temperature. The inlet

mass flow rate primarily influences the bulk Reynolds number which in return enhances turbulent flame speed. The experimental setup described above allows precise tuning of these variables. To illustrate their respective influence, five operating points are considered as displayed in table 1.

Table 1: Operating conditions utilized for investigation.

Case	\dot{m}_{total} [kg h ⁻¹]	T_{in} [°C]	Φ [-]	Re [-]	Re_t [-]	Da_t [-]
BSL	80.47	400	0.2	21463	69.1	1752
Φ	80.67	400	0.3	21555	69.4	1745
Re	60.35	400	0.2	16096	53.7	2254
$T_{\text{in},1}$	80.47	300	0.3	23971	76.1	2710
$T_{\text{in},2}$	80.47	200	0.3	27338	85.4	4610

Turbulent premixed combustion is categorized by its flame front behavior, specifically the reaction’s interaction with turbulence [13] [14]. Based on turbulent Reynolds and Damkoehler numbers different premixed combustion regimes are characterized. For the defined operating conditions the burner’s combustion behavior is placed in the quasi-steady corrugated flamelets regime ($Da_t \gg 1$ and $Re_t \gg 1$). In this regime turbulence-chemistry interaction mandates to be taken into account for all numerical calculations.

3. Numerical setup and theory

To numerically investigate the presented flame-anchoring mechanism, the fully compressible RANS-formulation of the Navier-Stokes equations is solved by the commercial CFD code Ansys Fluent in version 19.2. One of the challenges inherent to turbulent time-averaged combustion calculations is the determination of each species’s reaction rate. Since turbulence enhanced mixing processes affect those rates drastically, a modeling approach to calculate the species’ reaction source terms is utilized. The selected model is the eddy dissipation concept and is, besides a description of the general numerical setup, discussed in the following.

3.1. Numerical setup

To converge to a steady-state solution, a fully-coupled implicit solution procedure utilizing an algebraic multigrid pressure-based finite volume solver is applied. The pseudo-transient implicit under-relaxation formulation is employed for a stable and efficient convergence behavior. Spatial discretization is usually performed by the quadratic interpolation upwind (QUICK) scheme ensuring second order accuracy [15].

Alone the pressure equation is discretized by the PRESTO! scheme evaluating pressure at cell faces thus avoiding interpolation. The closure problem of the time-averaged Navier-Stokes equations is addressed by established ω -based eddy viscosity as well as Reynolds stress turbulence models. A detailed description is omitted at this point but has been addressed at length by other authors [16].

Although buoyancy may impact the shape of wall anchoring flames [17], gravity effects are assumed negligible. This deduces the assumption of axisymmetric flow conditions, which is confirmed by experiments. Albeit these express minute asymmetry which is more likely to be introduced by non-uniform total wall heat flux distribution than by buoyancy forces. Since heat conduction in the burner’s walls plays a major role in the flame anchoring mechanism [11], they are fully resolved by solving Fourier’s heat conduction equation.

Thermochemical fluid properties are evaluated by the CHEMKIN software libraries [18]. Therefore, heat capacity is assessed by a fourth order polynomial fit while heat conductivity, viscosity and molecular as well as thermal diffusion coefficients are derived from kinetic theory. Mixture averaging is performed for all transport properties except diffusion. Bruno et [19] concluded that multicomponent diffusion plays an essential factor in high Reynolds number reactive flows. Especially for hydrogen air mixtures and their inherently high diffusion coefficient of hydrogen, the overall flow field may be crucially impacted by differential diffusion [20]. Therefore, binary diffusion coefficients are calculated by the method of Dixon-Lewis and adapted into the flow by the Maxwell-Stefan diffusion equation. While the fluid’s properties are highly dependent on local flow state, solid material attributes are assumed constant and summarized in table 2.

Table 2: Solid material and radiation properties.

	ρ [kg m ⁻¹]	c_p [J kg ⁻¹ K ⁻¹]	λ [W m ⁻¹ K ⁻¹]	ϵ	f_d
Stainless steel	7900	750	25	0.8	0.5
Quartz glass	2200	740	1.38	0.8	0.1

Radiation phenomena may play a crucial role in the analysis of high temperature reacting flows. Therefore, the discrete ordinates model is applied to the presented configuration. The number of transport equations for radiation intensity depends on angular discretization, which is equal to 24 control angles in our case. The radiation energy transfer equation is solved in a sequential manner. All surfaces are considered to be gray walls. Special focus is put on quartz glass since it is considered the only non-opaque surface in the domain. That is why its transmission has to be taken in to account. In general, radiation is considered to be partially diffusive and partially specular. Internal emissivities ϵ and diffusive fractions f_d are listed in table 2.

The computational domain extends from 24 mm before the heating ring until the end of the glass tube. Therefore, radial fuel injection is not reflected in the simulation. In-

stead, the mixture is assumed to be perfectly premixed at domain inlet. This is verified by a cold gas mixing pre-study. By including of a long inlet in front of the mixture igniting flame holder, it is ensured that profiles of velocity, turbulent kinetic energy and its dissipation rate are fully developed before ignition. Temperature measurements on the symmetry axis at different axial locations, before and after the fuel injection, show that the isolation prevents heat transfer between the fluid and environment. Thus, temperature in front of the heating assembly is assumed constant and an adiabatic energy boundary condition can be applied.

To reflect the wall anchoring mechanism correctly, it is crucial to match the behavior of the heating ring assembly. To simplify the design, only the heating ring is considered as an simplified adjacent wall. In that way the physical phenomenon is still represented without the need to include the heating assembly's complicated geometry (Fig. 2). The isolation, which inhibits heat transfer to adjacent walls, is represented by an adiabatic boundary condition and missing wall connection. Applied boundary conditions are shown in figure 2.

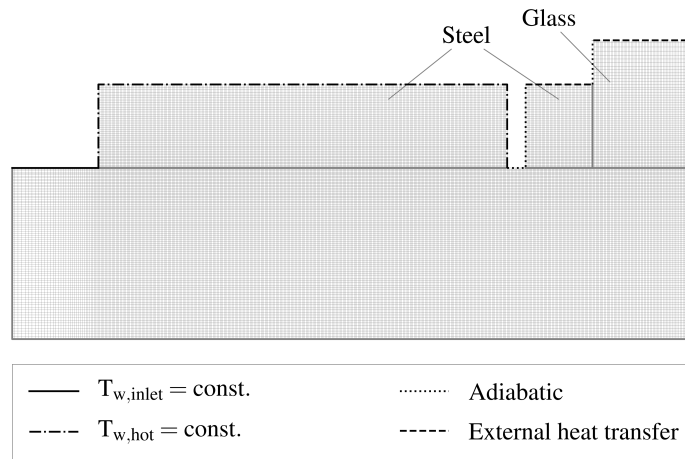


Figure 2: Grid and applied thermal boundary conditions.

The block structured hexahedral mesh is designed around two objectives: First and foremost the condition $y^+ \approx 1$ has to be met to resolve the turbulent wall boundary layer for all operating conditions. Secondly, the mesh has to be fine enough to determine the thin reaction zone and its quickly recombining intermediate species. To satisfy those demands the wall adjacent cell features a radial extend of $30\mu\text{m}$ and unity aspect ratio. While the aspect ratio is kept constant along the externally heated section, the cells grow exponentially in axial and radial direction as well as up- and downstream of it. This eventually amounts to $1.49 \cdot 10^6$ cells in total. A mesh study featuring finer grids, showed that smaller cell sizes do not impact numerical results.

3.2. Eddy dissipation concept

A critical challenge in turbulent RANS combustion simulations poses the correct calculation of each species' mean reaction rate. Since an evaluation utilizing an Arrhenius approach combined with mean flow quantities leads to significant deviations, a modeling strategy to incorporate turbulence-chemistry interaction must be applied [14]. One such model applicable to turbulent premixed flames is the eddy dissipation concept by Magnussen [21][22][23]. It is based on the analysis of turbulent scales in the energy cascade and may include arbitrarily complex reaction mechanisms. An extensive review comprising recent developments is available in [24] and recapitulated synoptically in this section.

In general and as basis for the EDC, the energy cascade hypothesis assumes that mechanical energy is continuously transformed from mean flow to the largest eddies, which subsequently pass it on to increasingly smaller eddies. In addition, it is expected that viscous dissipation mostly takes place within the smallest eddies, which are related to the Kolmogorov scales [16]. These timescales are furthermore connected to chemical reaction processes since they depict perfectly mixed species at a molecular level, a necessary condition for reaction processes. To transfer these presumptions into a numerical model, each computational cell is divided into a fine structure part of Kolmogorov scale length and a secondary segment representing the surrounding fluid. Consequently, the cell comprises a reacting part (fine structures) and a non-reacting one (surrounding fluid).

Typical length and velocity scales are assigned to the fine structure region and are denoted by L^* and u^* , which by definition are in the same order of magnitude as the Kolmogorov scales [25]. When setting the characteristic scales of the fine structures in relation to the turbulent flow scales, the fine structure length fraction γ_L is defined as

$$\gamma_L = \frac{u^*}{u'} = \left(\frac{3C_{D2}}{4C_{D1}^2} \right)^{1/4} \left(\frac{\nu\epsilon}{k^2} \right)^{1/4} \approx \frac{L^*}{L'}. \quad (1)$$

C_{D1} and C_{D2} are constants related to strain rate and energy transfer in the cascade model and designated to represent as many flow regimes as possible. For simplification, a directly proportional EDC modeling constant C_γ as well as the turbulent Reynolds number are introduced:

$$\gamma_L = C_\gamma \left(\frac{\nu\epsilon}{k^2} \right)^{1/4} = C_\gamma Re_t^{-1/4} \quad (2)$$

Since the fine structures also exchange mass with themselves, the mass fraction occupied by them within each cell is redefined as $\gamma^* = \gamma_L^2$ instead of the natural choice $\gamma^* = \gamma_L^3$ [22]. Then, the mass transfer rate between fine structures and their surrounding fluid, in relation to the fine structure mass, is expressed by

$$\dot{m}^* = 2 \frac{u^*}{L^*} = \left(\frac{3}{C_{D2}} \right)^{1/2} \left(\frac{\epsilon}{\nu} \right)^{1/2}. \quad (3)$$

Therefore, the characteristic time scale of fine structures is denoted by

$$\tau^* = \frac{1}{\dot{m}^*} = \left(\frac{C_{D2}}{3}\right)^2 \left(\frac{\nu}{\epsilon}\right)^{1/2}, \quad (4)$$

which again may be rewritten in terms of a linear constant C_τ and turbulent Reynolds number:

$$\tau^* = C_\tau \left(\frac{\epsilon}{\nu}\right)^{1/2} = C_\tau Re^{-1/2} \frac{k}{\epsilon} \quad (5)$$

Default values of the EDC constants equal $C_\gamma = 2.1366$ and $C_\tau = 0.4082$. By application of the fine structure mass fraction, the mean mass transfer rate in relation to total mass, which can be understood as the mean rate of molecular mixing [25], is derived as

$$\dot{m} = \dot{m}^* \gamma^* = \frac{\gamma_L^2}{\tau^*}. \quad (6)$$

Mean fluid quantities are expressed by linear combination

$$\bar{\Psi} = \Psi^0(1 - \gamma_L^3) + \Psi^* \gamma_L^3. \quad (7)$$

Where superscript 0 denotes properties of the surrounding fluid in each cell. Utilizing this formulation the species' mass fractions are expressed by

$$Y_i^0 = \frac{\bar{Y}_i - Y_i^* \gamma_L^3}{1 - \gamma_L^3}. \quad (8)$$

When Y_i^* corresponds to species mass fraction in the fine structure region after numerical integration of all chemical reactions, the individual reaction of each specie is expressed as

$$\bar{\omega}_i = \bar{\rho} \dot{m} \chi (Y_i^* - Y_i^0). \quad (9)$$

While χ denotes fraction of fine structures that actually participate in the reaction and is usually assumed to unity. Substitution of equations (6) and (8) yields the reaction rate depending on mean quantities as

$$\bar{\omega}_i = \bar{\rho} \frac{\gamma_L^2}{\tau^*(1 - \gamma_L^3)} (Y_i^* - \bar{Y}_i). \quad (10)$$

The most computationally expensive task of reactive flow simulations is numerical integration of chemical kinetics. To improve this limitation, the reacting fine structure region is solved by a zero-dimensional model. Originally, a perfectly stirred reactor (PSR) was proposed for this [21]. It features an isothermal and isobaric set of ODEs, which is solved to steady-state. Due to the persisting extensive numerical cost for this operation, the selected solver follows a different approach by neglecting mixing between fine structures and surrounding to form a simplified set of ODEs referred to as a plug flow reactor (PFR) [24]. Instead of finding a steady state solution, the PFR ODE system is only integrated for the fine structure time scale τ^* . Boesenhofer [24] pointed out that there are only minor differences in accuracy.

Two limiting scenarios have to be considered when looking at wall bounded flows in combination with the EDC combustion model. Since turbulent kinetic energy approaches zero at the wall, γ_L advances towards infinity which has to be omitted. An elegant solution to eliminate this behavior is to apply blending functions for γ_L depending on Re_t [26]. A more straightforward approach is to apply a limiter onto γ_L , which performs comparably well and is thus applied [26].

A second singularity similar to the first one is encountered when γ_L approaches unity. This corresponds to solely fine structures in a cell and a species' reaction rate approaching infinity. De [27] came to the conclusion that the EDC changes the mean species mass fraction by linear relaxation, thus avoiding the complex nonlinear problem. In this context the relation of the linear mixing problem's timescale is described as

$$\frac{\tau^*}{\tau_{mix}} = \frac{\gamma_L^2}{1 - \gamma_L^3} < 1. \quad (11)$$

Therefore, the stability condition and limiting value for the fine structure mass fraction, which requires the reaction time τ^* to be smaller than the mixing time scale, equals $\gamma_L = 0.755$.

As the flame-wall interaction (FWI) mode of the configuration is sidewall quenching (SWQ), reactions right at the wall have to be inhibited to reflect physical quenching of the flame. Since the EDC model is not able to account for this effect and instead assigns the described limiter, the reaction is inhibited by setting the reactions source terms to zero in all wall adjacent cells. Although default EDC modeling constants perform well in a broad application range, they are modified to fit all operating conditions of the featured reactive flow as accurately as possible. An increased constant value of $C_\gamma = 3.0$ results in a better agreement to most experimental measurements. The same value is already reported in [27].

4. Reaction kinetic analysis

Before conducting a detailed numerical investigation featuring finite rate chemistry a review of available reaction mechanisms is worthwhile. For that purpose, chemical kinetics are evaluated in a simplified canonical configuration corresponding to a steady one-dimensional premixed flame. To ensure that each chemical kinetic is able to reproduce the central physical phenomenon of the configuration, it has to be part of the canonical problem as well [11]. In the featured setup flame shape, position and extinction behavior are particularly determined by heat transfer processes at the wall. Therefore, the investigation of reaction mechanisms includes non-adiabatic premixed flame calculations under heat loss conditions. Although hydrogen/air kinetics have been explored for an number of different applications [28] [29] [30], there is no study jet focusing on the influence of heat loss.

For comparison five reaction mechanisms are taken into account. Four of them are considered detailed (Konnov [31], Li [32], UCSD [33], USC [34]) while the final one is reduced (Boivin [35]). They collectively feature four identical major species (H_2 , O_2 , N_2 , H_2O) as well as five minor ones (OH , H_2O_2 , H , O , HO_2). The number of reactions varies from 12 to 29. Due to their much larger chemical time scale, nitrogen reactions

are neglected in all calculations. A more detailed perspective on the different kinetics is summarized in table 3. One of the key differences is that the simplified mechanism comprises irreversible reactions while all detailed ones refrain from it.

The experimental test setup allows for OH^* chemiluminescence measurements. That is why in addition to hydrogen oxidation, an OH^* chemiluminescence sub-mechanism has to be included into the overall reaction kinetic. For the study at hand, the sub-mechanism of Kathrotia [36] is incorporated.

Table 3: Properties of investigated hydrogen/air reaction mechanisms.

	N_{Total}	$N_{\text{Fall-off}}$	N_{Pressure}	$N_{\text{Irreversible}}$
Konnov [31]	29	4	4	0
Li [32]	21	2	4	0
UCSD [33]	23	2	4	0
USC [34]	25	2	4	0
Boivin [35]	12	2	2	6

The simplified numerical formulations are solved by the Cantera laminar reacting flow solver [37]. The initial problem of reduced complexity is an adiabatic one-dimensional freely propagating flame. This configuration is well suited to examine laminar flame speed as an inherent property of reaction kinetics. The influence of equivalence ratio on laminar flame velocity is depicted and compared to its experimental counterpart in figure 3. At standard conditions the deviation between experiment and numerical calculations for all featured mechanisms, lie within the usually reported error margin. It should be noted that all simplified calculations are carried out under atmospheric pressure conditions since the impact of pressure variations in the burner setup are considered subordinate. The series is repeated for elevated unburnt mixture temperatures to investigate settings closer to the actual operating conditions. As detailed in figure 3 there are only minor differences for lean flame fronts ranging from $\Phi = 0.2$ to $\Phi = 0.3$. Over the entire equivalence ratio scope the largest disparity is observed between the detailed Konnov and reduced Boivin chemical kinetics.

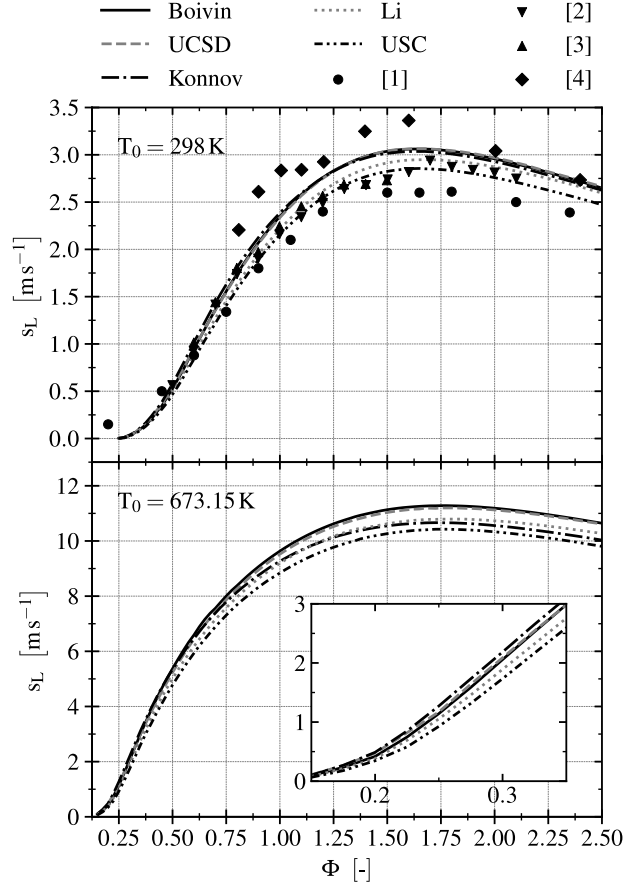


Figure 3: Laminar flame speed results for varying unburnt gas temperatures. Applied linestyles are valid for all plots in this section.

Since wall heat transfer and subsequent quenching reflect the major physical phenomenon, a canonical configuration incorporating these effects is analyzed. For this purpose the energy equation of the laminar flame solver is altered to incorporate an additional heat sink term. In fact, the heat sink is realized by introducing a heat loss factor γ_{loss} to the already implemented heat of reaction source term. Therefore, the complete energy equation in mixture fraction space is expressed by:

$$\bar{\rho} \bar{c}_p u \frac{dT}{dZ} = \frac{d}{dZ} (\bar{\lambda} \frac{dT}{dZ}) - \sum_k^{n_k} j_k c_{p,k} \frac{dT}{dZ} - (1 - \gamma_{loss}) \sum_k^{n_k} h_k W_k \dot{\omega}_k \quad (12)$$

By inclusion of this heat loss factor only the reaction front of the premixed flame is impacted while the remaining flame remains unaltered [38].

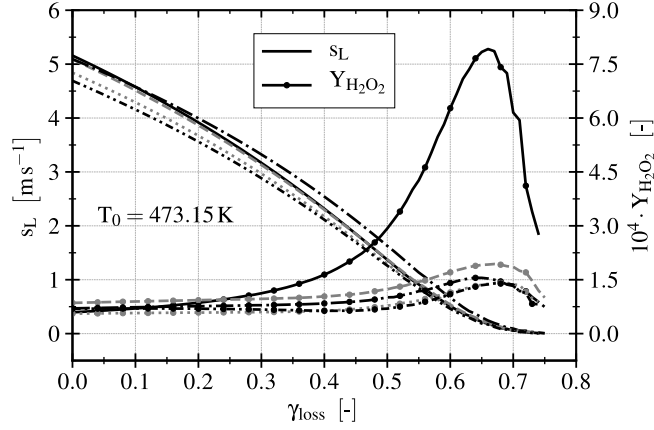


Figure 4: Laminar flame speed under the influence of external heat loss.

Figure 4 depicts the influence of the established heat loss factor on laminar flame velocity as well as hydrogen peroxide concentration as an intermediate species. In general, quenching is observed at a heat loss factor of $\gamma_{\text{loss}} = 0.745$. Discrepancies in laminar flame speed between the applied chemical kinetics become smaller as the extinction point is approached. Contradictorily, deviations of H_2O_2 mass fraction between detailed and the simplified mechanisms intensifies for higher heat loss factors. This effect is further investigated in figure 5 with help of a non-dimensional variable to simplify visualization of the narrow reaction zone:

$$\xi = \frac{x - x_{ff}}{\Delta_{ff}} \quad (13)$$

Where x_{ff} and Δ_{ff} denote the flame front's positions as well as thickness. Figure 5 visualizes minor species H, OH and H_2O_2 under adiabatic and non-adiabatic imposed heat loss conditions. The first two species plots show a clear trend of diminished intermediate species concentration under heat loss conditions. Albeit that, the reactions kinetics behave fairly similar. This again changes for the hydrogen peroxide. First, additional heat loss does not seem to significantly alter the maximum species concentration when any of the detailed kinetics is employed. A second observation is that the maximum H_2O_2 mass fraction under heat loss conditions is about four times higher with the simplified mechanism compared to detailed ones.

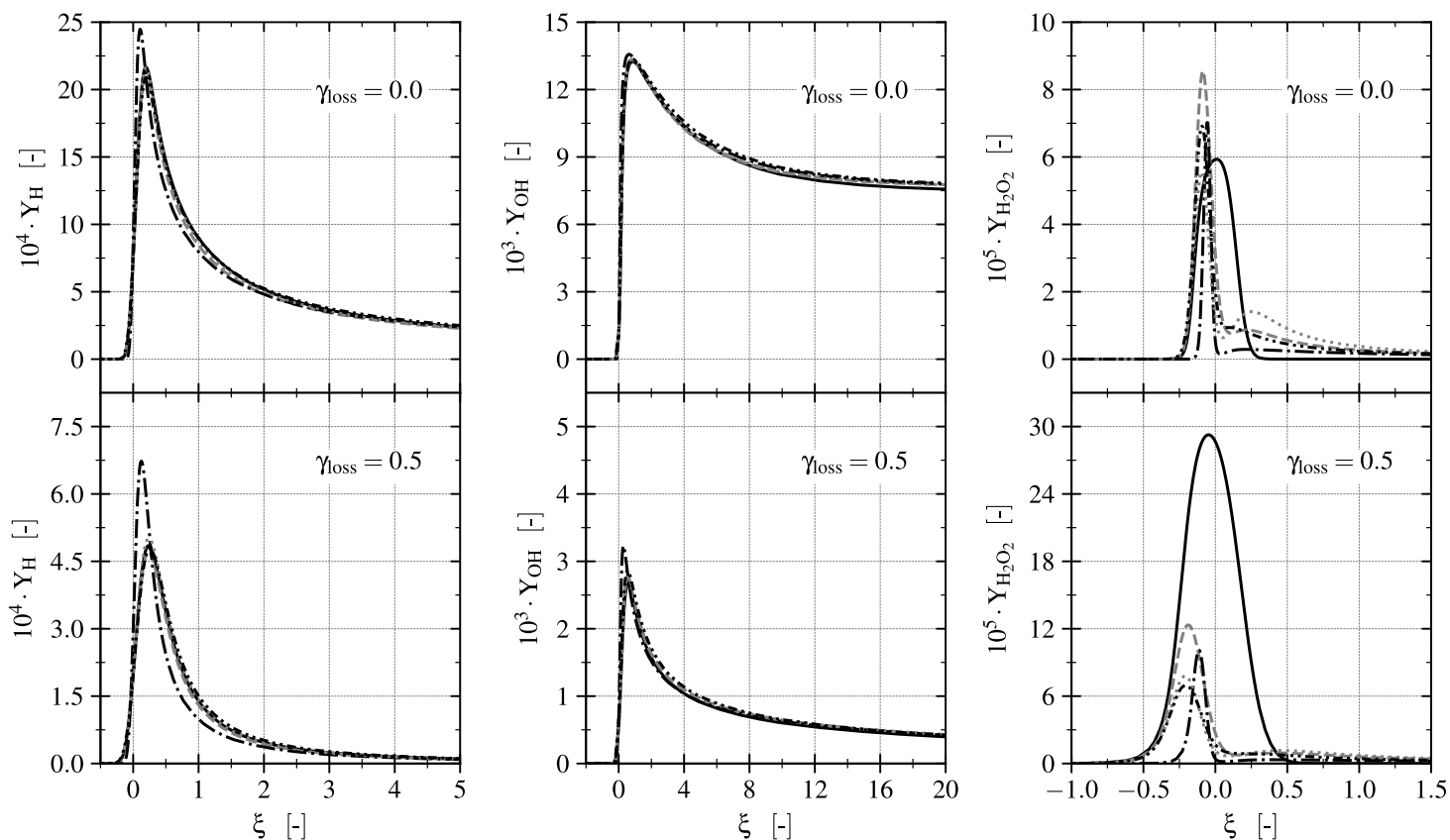


Figure 5: Minor species' mass fractions under adiabatic and non-adiabatic conditions ($\gamma_{\text{loss}} = 0.5$)

Although the skeletal mechanism of Boivin performs comparably well in adiabatic calculations, it demonstrated discrepancies for minor species under heat loss conditions. Therefore, the much more computationally expensive UCSD reactions mechanism is selected for the numerical study. It should be noted that the other detailed chemical kinetics perform very similar to the UCSD mechanism. Therefore, together with the chemiluminescence reactions ten species and 31 reactions considered in all consecutive simulations.

5. Numerical study and results

This section presents a detailed investigation of wall anchoring turbulent flame fronts by rigorous comparison of numerical and experimental results. Chemiluminescence of the OH^* radical is utilized to bring measurements and calculations together. Thus, qualitative alignment of the numerical method may be validated. After a comprehensive review of the flame front's interaction with the wall by SWQ, the influence of various RANS-based turbulence models on numerical results is assessed. Finally,

the applicability of the numerical method over a wide range of operating conditions is evaluated.

5.1. Flame anchoring phenomenon

As briefly discussed in section 1, steady flame anchoring at walls is introduced by interaction of reaction products and reactants with adjacent walls. When taking a closer look it becomes clear that hot reaction products transfer heat into the wall downstream of the flame front, which in return induces heat conduction within the solid. This transport process is responsible for increasing the wall's temperature upstream of the flame front, which leads to enhanced thermal transfer into the fluid at this position. Therefore ignition of the unburnt gas is encouraged. The described phenomenon by itself may already lead to steady flame anchoring. External heating of a wall segment enhances the anchoring process and forces it to take place at a specific location. In the numerical setup this behavior is imposed by application of constant temperature boundary conditions at all heated wall segments (Fig. 2). Thus, all heat introduced into the heating ring can only escape back into the fluid.

Figure 6 displays this behavior by visualizing wall temperature, heat of reaction as well as velocity streamlines. Due to disparate temperature scales between externally heated and all other resolved walls, the temperature distribution is normalized separately. Red isolines depict 10 % of the maximum heat release rate and therefore respond to the beginning and end of the reaction zone. As most featured operating conditions (Tab. 1) include hot wall temperatures of 800 K, figure 6 shows a wall anchoring flame for these conditions. It may be inferred that at excessive wall temperatures, the unburnt mixture is ignited immediately at the beginning of the heated segment. Under these conditions additional heat conduction through the wall, induced by the hot flame, seems to be redundant. But, elevated wall temperatures enhance the reaction's flammability limits and thus lead to a more stable anchoring flame. Although the influence of external heating means on the flame anchoring position is obvious, its influence on flame shape as well as general flame structure seems to be negligible. That's justified by evaluating major species distributions as well as the flow field. Therefore and for cases where flow and turbulent flame speed match reasonably well, external wall heating can be applied as a means of controlled thermal flame anchoring.

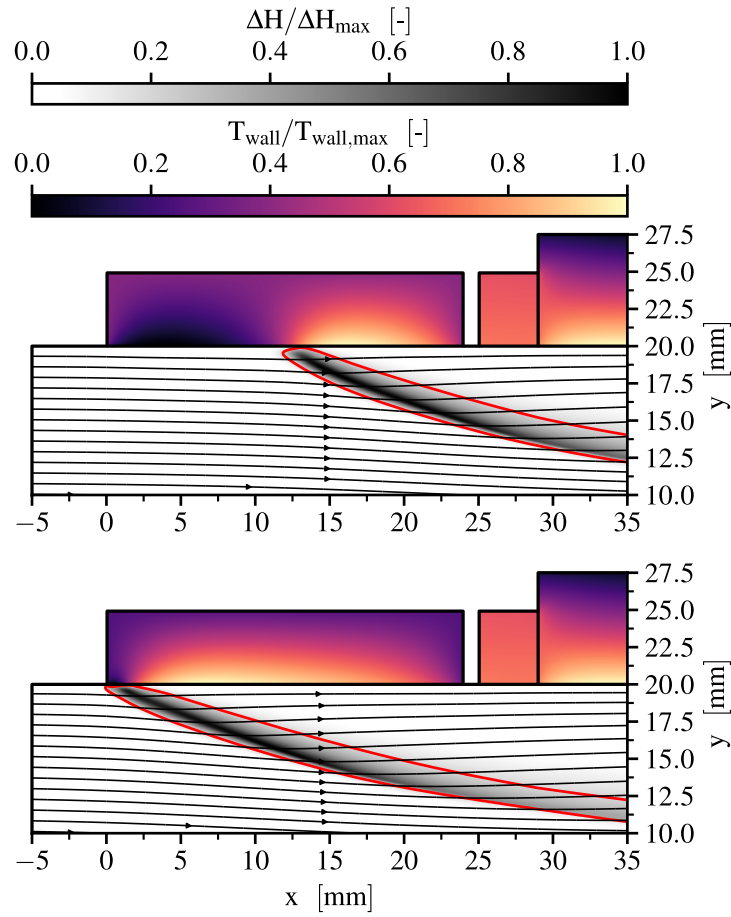


Figure 6: Flame wall interaction for a hot wall temperature of $T_{w,hot} = 700^\circ\text{C}$ (top) and $T_{w,hot} = 800^\circ\text{C}$ (bottom). The numerical setting reflects the baseline case.

The general flame shape and structure is displayed in figure 7 by depicting gas mixture temperature and various species distributions. To demonstrate their differences, the major species H_2O , minor species OH as well as the quickly recombining minor species H are portrayed.

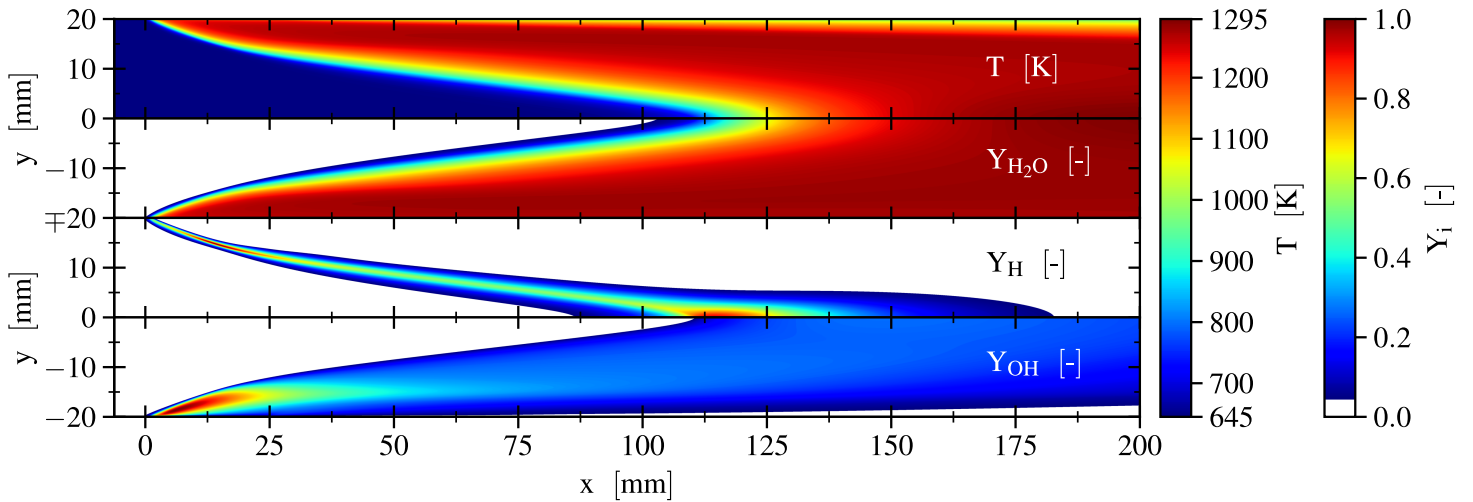


Figure 7: General flame structure for the same numerical setup as in figure ??.

5.2. RANS-based turbulence modeling

To solve the closure problem of time-averaged Navier-Stokes equations, multiple RANS turbulence models are applied to the baseline operating condition. A detailed performance evaluation is given in the following.

Two-equation turbulence models have been successfully applied in RANS simulations of premixed combustion [5]. This work aims to extend the assessment of turbulence models in cooperation with the EDC for wall anchoring flames under SWQ conditions. Due to their inherent ability to accurately resolve turbulent boundary layers, only ω -based models are chosen for the study at hand. For this purpose the standard, baseline (BSL) and shear stress transport (SST) k - ω models are selected as classical two-equation models. In addition, one ω -based Reynolds stress turbulence model featuring five transport equations is evaluated as well. In conclusion, the investigated RANS turbulence models are: k - ω std, k - ω BSL, k - ω SST and stress- ω RSM model. For all ω -based turbulence models, which can be integrated through the entire viscous sub-layer, wall treatment is identical as well as y^+ -sensitive. Since all deployed mesh resolutions satisfy the $y^+ \leq 1$ condition, no turbulent wall functions are applied at any point.

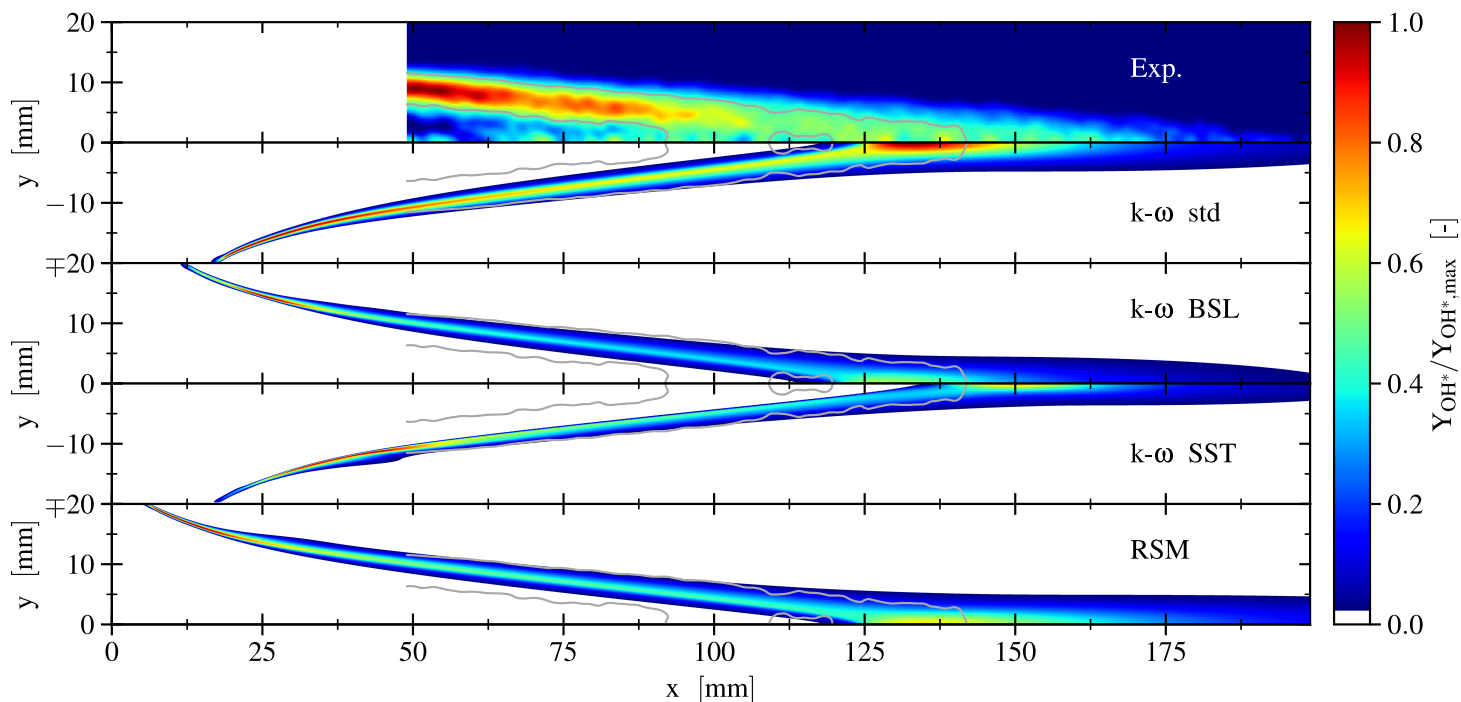


Figure 8: Influence of RANS-based turbulence models. Setup corresponds to baseline case. Experimental results are visualized by inverse Abel transformation. Grey lines correspond to iso-values of 0.5.

A qualitative comparison of Abel inversed experimental measurements and simulation results featuring different turbulence models is depicted in figure 8. Reasonably well accuracy is achieved by all employed turbulence models. One major difference concerns varying flame anchoring positions. This is displayed in more detail in figure 9 by plotting total surface heat flux over the heated wall segment. It shows that there is only a minor discrepancy between $k-\omega$ std and $k-\omega$ SST models while $k-\omega$ BSL and RSM model differ significantly.

A second major dissimilarity involves the location of the maximum concentration of the OH^* chemiluminescence radical. Except for the $k-\omega$ std model, the employed turbulence models predict the maximum location at the flame anchoring position. This is in accordance with the inverse Abel transformed experimental data. In contrast, the $k-\omega$ std model computes the maximum location to be at the flame's tip and thus symmetry line. The same behavior is visualized by the distribution of the H mass fraction at the axis of symmetry (Fig. 10).

Especially, the $k-\omega$ BSL and RSM, which promises to be the most accurate turbulence model directly calculating the Reynolds stress tensor's components, behave remarkably similar. Since the $k-\omega$ SST model features a much thinner flame reaction zone and due to extensive computational cost of the RSM model, the $k-\omega$ BSL model is conclusively evaluated to perform superior. That is why all subsequent simulations feature it as a RANS-based turbulence modeling technique.

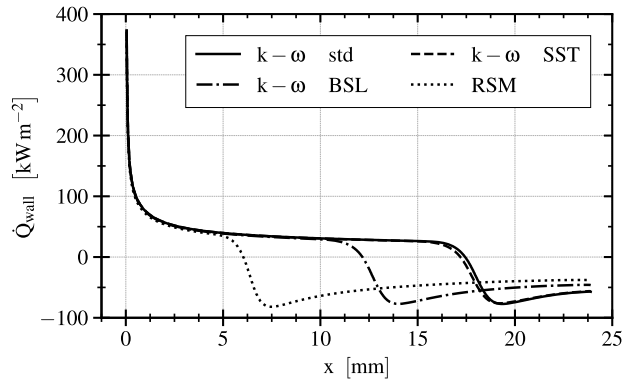


Figure 9: Surface heat flux on externally heated wall segment for different turbulence models.

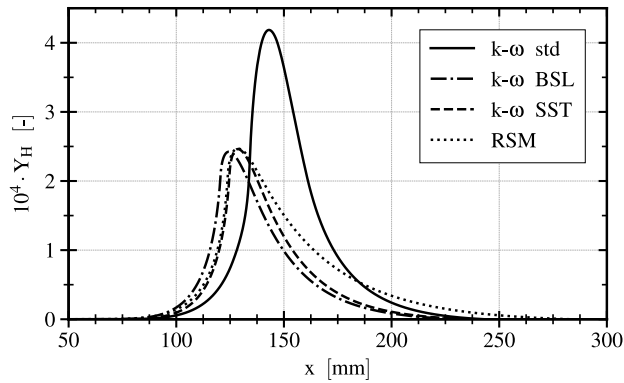


Figure 10: Distribution of hydrogen atom concentration at the flame's symmetry line.

5.3. Operating conditions

A comparison of experimental measurements and numerical calculations for a wide operational range is discussed. Featured operating points are summarized in table 1. The influence of three main quantities is under investigation: equivalence ratio, bulk Reynolds number and unburnt mixture temperature.

Results showing the impact of an increased in equivalence ration as well as a decrease in bulk Reynolds number are visualized in figure 11. By merely raising hydrogen mass fraction at inlet, the equivalence ratio is adjusted from $\Phi = 0.2$ to $\Phi = 0.3$. This induces a greater flame speed which results in a shortened flame length. Actually, the flame becomes so compressed that only the flame's tip is visible in the glass tube's measurement section. This unfortunately inhibits any application of the inverse Abel transformation. Therefore, numerical results are compared to symmetrically averaged but otherwise unaltered chemiluminescence measurements. These solely depict the end of the reaction zone. By these presumptions, only minor deviations in flame length and reaction zone location are evident.

The bottom illustration of figure 11 depicts a reduction in Reynolds number from 20000 in the baseline case (Fig. 8) to only 15000 by diminishing inlet mass flow rate. Again, the total flame length is inhibited, but not as much as in the previous equivalence ratio determined case. Therefore, an inverse Abel transformation remains possible without any repercussions. Again the qualitative comparison shows good agreement for the chemiluminescence distribution.

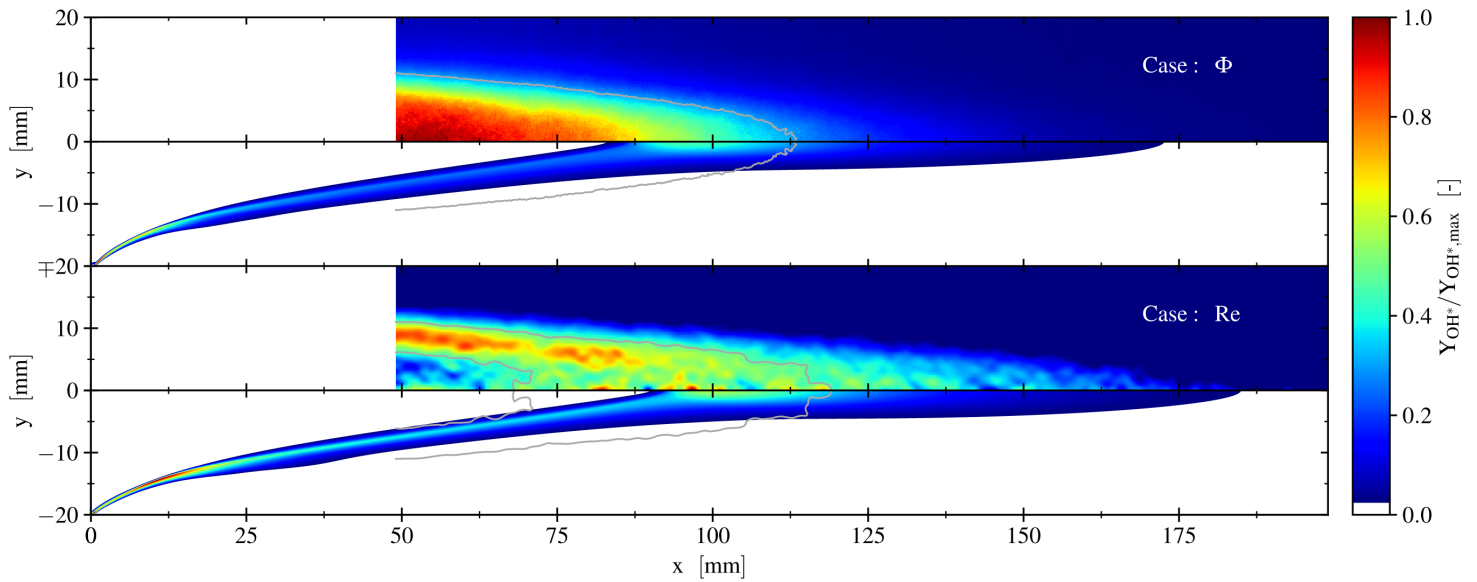


Figure 11: Influence of equivalence ratio and bulk Reynolds number depicted by simulation as well as Abel inversed chemiluminescence measurements.

Finally, two operating points featuring colder temperatures of the unburnt gas are discussed. Such an enthalpy reduction of the mixture culminates in much lower turbulent flame speeds and thus elongated flames. This behavior is clearly depicted for numerical and experimental results (Fig. 12). Compared to the previously discussed operating conditions, the simulations predict a slightly longer flame front than observed in corresponding experiments. Although not critical, this could be remedied by further increasing the C_γ EDC constant.

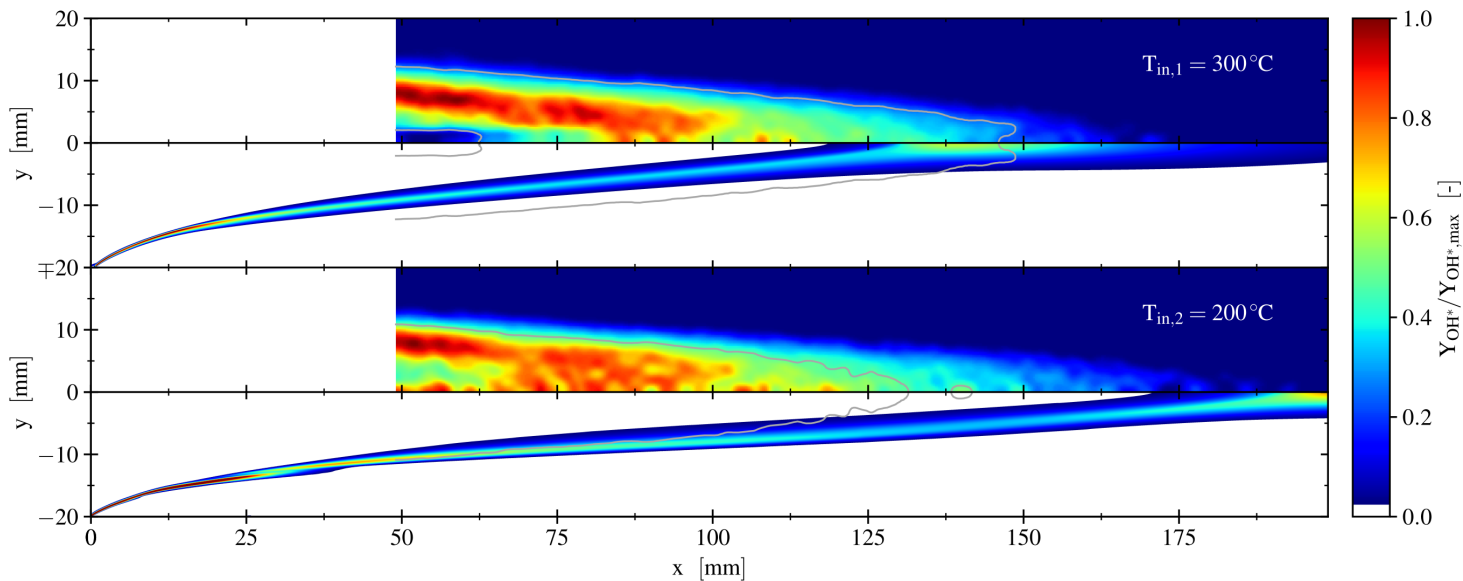


Figure 12: Influence of unburnt mixture temperature depicted by simulation as well as Abel inversed chemiluminescence measurements.

6. Conclusions

A thermal flame holder design suitable for continuous combustion devices has been studied experimentally and numerically. Different operating conditions as well as RANS-based turbulence models are evaluated. A preceding chemical kinetics investigation including the influence of quenching by heat loss has been conducted. In conclusion there are only minor discrepancies between all featured detailed reaction mechanisms. A reduced kinetic performed comparably well but expressed some significant deviations under heat loss conditions.

Qualitative OH^* chemiluminescence comparisons show that the applied numerical method is able to predict the general flame shape quite well. For the EDC combustion model an increased modeling constant of $C_\gamma = 3.0$ provides superior agreement. This holds true for various inlet mass flow rates, and thus bulk Reynolds numbers, as well as equivalence ratios. Solely for extensively elongated flames by diminishing unburnt mixture temperatures, deviations between experiment and numerics become more pronounced.

7. Acknowledgements

The authors gratefully acknowledge the Gauss Centre for Supercomputing e.V. (www.gauss-centre.eu) for funding this project by providing computing time on the GCS Supercomputer SuperMUC at Leibniz Supercomputing Centre (www.lrz.de).

References

References

- [1] J. Wan, H. Zhao, Anchoring mechanisms of methane/air premixed flame in a mesoscale diverging combustor with cylindrical flame holder, *Fuel* 232 591–599.
- [2] C. Fureby, Large eddy simulation of combustion instabilities in a jet engine afterburner model, *Combustion Science and Technology* 161 (2000) 213–243. doi : 10 . 1080/00102200008935818.
- [3] M. R. Gruber, R. A. Baurle, T. Mathur, K. Y. Hsu, Fundamental studies of cavity-based flameholder concepts for supersonic combustors, *Journal of Propulsion and Power* 17 (2001) 146–153.
- [4] A. Ben-Yakar, R. K. Hanson, Cavity flame-holders for ignition and flame stabilization in scramjets: An overview, *Journal of Propulsion and Power* 17 (2001) 869–877.
- [5] J. Wan, A. Fan, H. Yao, W. Liu, Flame-anchoring mechanisms of a micro cavity-combustor for premixed h₂/air flame, *Chemical Engineering Journal* 275 17–26.
- [6] K. S. Kedia, A. F. Ghoniem, The anchoring mechanism of a bluff-body stabilized laminar premixed flame, *Combustion and Flame* 161 2327–2339.
- [7] M. Brouillette, M. Picard, D. Rancourt, J. S. Plante, Shock-induced combustion and its applications to power and thrust generation, in: *30th International Symposium on Shock Waves 1*, Springer, 2017, pp. 53–58.
- [8] J. Dunmon, S. Sobhani, M. Wu, R. Fahrig, M. Ihme, An investigation of internal flame structure in porous media combustion via x-ray computed tomography, *Proceedings of the Combustion Institute* 36 (2017) 4399–4408. doi : http : //dx . doi . org/10 . 1016/j . proci . 2016 . 06 . 188.
- [9] M. Sanches-Sanz, D. Fernandez-Galisteo, V. N. Kurdyumov, Effect of the equivalence ratio, danckler number, lewis number and heat release on the stability of laminar premixed flames in microchannels, *Combustion and Flame* 161 (2014) 1282–1293.
- [10] K. Maruta, T. Kataoka, N. I. Kim, S. Minaev, R. Fursenko, Characteristics of combustion in a narrow channel with a temperature gradient, *Proceedings of the Combustion Institute* 30 (2005) 2429–2436.
- [11] K. Bioche, G. Ribert, L. Vervisch, Simulating upstream flame propagation in a narrow channel after wall preheating: Flame analysis and chemistry reduction strategy, *Combustion and Flame* 200 (2019) 219–231. doi : https : //doi . org/10 . 1016/j . combustflame . 2018 . 11 . 028.
- [12] K. Y., T. T., An experimental study on stability and combustion characteristics of an excess enthalpy flame, *Proceedings of the Combustion Institute* 19 (1982) 1503–1509. doi : https : //doi . org/10 . 1016/S0082-0784 (82) 80327-5.

- [13] N. Peters, The turbulent burning velocity for large-scale and small-scale turbulence, *Journal of Fluid Mechanics* 384 107–132.
- [14] T. Poinso, D. Veynante, *Theoretical and Numerical Combustion*, 2nd Edition, R.T. Edwards, Inc., 2005.
- [15] B. P. Leonhard, A stable and accurate convective modelling procedure based on quadratic upstream interpolation, *Computer Methods in Applied Mechanics and Engineering* 19 (1979) 59–98. doi:[https://doi.org/10.1016/0045-7825\(79\)90034-3](https://doi.org/10.1016/0045-7825(79)90034-3).
- [16] S. S. Pope, *Turbulent flows*, 1st Edition, Cambridge University Press, 2000.
- [17] K. Bioche, G. Ribert, L. Vervisch, The role of gravity in the asymmetry of flames in narrow combustion chambers, *Combustion and Flame* 203 (2019) 238–246. doi:<https://doi.org/10.1016/j.combustflame.2019.02.020>.
- [18] Chemkin, Chemkin, <http://combustion.ucsd.edu> (2019).
- [19] C. Bruno, V. Sankaran, H. Kolla, J. H. Chen, Impact of multi-component diffusion in turbulent combustion using direct numerical simulations, *Combustion and Flame* 162 (2015) 4313–4330. doi:<http://dx.doi.org/10.1016/j.combustflame.2015.07.013>.
- [20] J. Chen, R. Sankaran, E. Hawkes, Characterization of differential diffusion effects during the constant volume ignition of a temperature stratified lean premixed hydrogen/air mixture subject to decaying turbulence, in: *Fall meeting of the western states section of the combustion institute*, 2007.
- [21] B. F. Magnussen, On the structure of turbulence and a generalized eddy dissipation concept for chemical reaction in turbulent flow, in: *19th Aerospace Sciences Meeting*, 1981. doi:<https://doi.org/10.2514/6.1981-42>.
- [22] B. F. Magnussen, Modeling of nox and soot formation by the eddy dissipation concept, in: *International Flame Research Association First Topic Oriented Technical Meeting*, 1989.
- [23] I. R. Gran, B. F. Magnussen, A numerical study of a bluff-body stabilized diffusion flame. part 2. influence of combustion modeling and finite-rate chemistry, *Combustion Science and Technology* 119 (1996) 191–217. doi:<https://doi.org/10.1080/00102209608951999>.
- [24] M. Bsenhofer, E.-M. Wartha, C. Jordan, M. Harasek, The eddy dissipation concept - analysis of different fine structure treatments for classical combustion, *Energies* 11. doi:<https://doi.org/10.3390/en11071902>.
- [25] I. S. Erstesvag, B. F. Magnussen, The eddy dissipation turbulence energy cascade model, *Combustion Science and Technology* 159 (2000) 213–235.
- [26] T. Myhrvold, *Combustion modeling in turbulent boundary layer flows*, Ph.D. thesis, Norwegian University of Science and Technology (2003).

- [27] A. De, E. Oldenhof, P. Sathiah, D. Roekaerts, Numerical simulation of delft-jet-in-hot-coflow (djhc) flames using the eddy dissipation concept model for turbulencechemistry interaction, *Flow Turbulence Combustion* 87 537–567.
- [28] B. Liu, G.-Q. He, F. Qin, J. An, S. Wang, L. Shi, Investigation of influence of detailed chemical kinetics mechanisms for hydrogen on supersonic combustion using large eddy simulation, *International Journal of Hydrogen Energy* 44 (2019) 5007–5019. doi:<https://doi.org/10.1016/j.ijhydene.2019.01.005>.
- [29] A. Vincent-Randonnier, V. Sabelnikov, A. Ristori, N. Zettervall, C. Fureby, An experimental and computational study of hydrogen-air combustion in the lapcat ii supersonic combustor, *Proceedings of the Combustion Institute* 37 (2019) 3703–3711. doi:<https://doi.org/10.1016/j.proci.2018.05.127>.
- [30] P. P. Kumar, K.-S. Kim, S. Oh, J.-Y. Choi, Numerical comparison of hydrogen-air reaction mechanisms for unsteady shock-induced combustion applications, *Journal of Mechanical Science and Technology* 29 (2015) 893–898. doi:DOI10.1007/s12206-015-0202-2.
- [31] V. A. Alekseev, M. Christensen, A. A. Konnov, The effect of temperature on the adiabatic burning velocities of diluted hydrogen flames: A kinetic study using an updated mechanism, *Combustion and Flame* 162 (2015) 1884–1898. doi:10.1016/j.combustflame.2014.12.009.
- [32] J. Li, Z. Zhao, A. Kazakov, F. L. Dryer, An updated comprehensive kinetic model of hydrogen combustion, *International Journal of Chemical Kinetics* (2004) 566–575doi:<https://doi.org/10.1002/kin.20026>.
- [33] F. Williams, U. of California at San Diego, Chemical-kinetic mechanisms for combustion applications, <http://combustion.ucsd.edu> (2019).
- [34] S. G. Davis, A. V. Joshi, H. Wang, F. Egolfopoulos, An optimized kinetic model of h₂/co combustion, *Proceedings of the Combustion Institute* 30 1283–1292.
- [35] P. Boivin, Reduced-kinetic mechanism for hydrogen and syngas combustion including autoignition (2011).
- [36] T. Kathrotia, M. Fikri, M. Bozkurt, M. Hartmann, U. Riedel, C. Schulz, Study of the hom reaction forming oh kinetics of oh chemiluminescence in hydrogen combustion systems, *Combustion and Flame* 157 (2010) 1261–1273. doi:doi:10.1016/j.combustflame.2010.04.003.
- [37] D. G. Goodwin, R. L. Speth, H. K. Moffat, B. W. Weber, Cantera: An object-oriented software toolkit for chemical kinetics, thermodynamics, and transport processes, <https://www.cantera.org>, version 2.4.0 (2018). doi:10.5281/zenodo.1174508.
- [38] F. Proch, A. M. Kempf, Modeling heat loss effects in the large eddy simulation of a model gas turbine combustor with premixed flamelet generated manifolds, *Proceedings of the Combustion Institute* 35 (2015) 3337–3345. doi:<https://doi.org/10.1016/j.proci.2014.07.036>.